Materials Horizons

Accepted Manuscript

This article can be cited before page numbers have been issued, to do this please use: L. Xu, H. Y. Liu, Q. Song, X. Sun, Z. Zhao, Z. Ge, Y. Chen, X. Jiang and L. Jiang, *Mater. Horiz.*, 2025, DOI: 10.1039/D5MH01249J.




ROYAL SOCIETY OF CHEMISTRY

rsc.li/materials-horizons

View Article Online
DOI: 10.1039/D5MH01249J



## New concepts

Inspired by the ionic transport mechanisms of biological olfaction, this work introduces a paradigm shift in gas sensing, realizing nanoconfined solvated ion transport within hierarchical porous membranes. Conventional electronic gas sensors suffer from intrinsic limitations in sensitivity, power efficiency, and humidity susceptibility. To overcome this, we engineer bioinspired ionic membranes by confining ionic liquid within amino-functionalized graphene oxide frameworks, faithfully emulate biological ion channels. The unique hierarchical tremella morphology significantly expands gas diffusion pathways and provides optimized interaction sites for volatile organic compounds. This architecture utilizes the transport of solvated ions as the signal transduction mechanism, thereby fundamentally overcoming the drawbacks of electronic signal-based sensors. The resulting membranes exhibit exceptional sensing performance of ultra-low detection limit (189 ppb), high sensitivity (2.02%/ppm), specific ethanol selectivity, outstanding reversibility (>100 cycles, 88.92% retention), and ultralow power consumption (0.28 μW per response). Importantly, the solvated ion transport mechanism ensures reliable applications across a wide humidity range, as demonstrated in real-world applications ranging from food spoilage detection (40% RH) to breath alcohol monitoring (90% RH). This concept of bioinspired gas sensing via nanoconfined solvated ion transport provides a scalable blueprint for next-generation, energy-efficient gas sensing devices, enabling practical application in complex and real-world environments.

DOI: 10.1039/D5MH01249J

# Solvated Ion Transport in Hierarchical Tremella-like Ionic Membranes for Low-Power and High-Sensitivity Ethanol Sensing

Lingyun Xu,[a] Hongyang Liu,[a] Qi Song,[a] Xiaohan Sun,[a] Zhihao Zhao,[a] Zhenya Ge,[a] Yupeng Chen,*[bc] Xiangyu Jiang,*[d] and Lei Jiang[ef]

[a] School of Chemistry, Beihang University, Beijing 100191, China.

[b] CAS Key Laboratory for Biomedical Effects of Nanomaterials and Nanosafety, CAS Center for Excellence in Nanoscience, National Center for Nanoscience and Technology, Beijing 100190, China.

[c] College of Materials Science and Technology, Beijing Forestry University, Beijing 100083, China.

[d] International Research Institute for Multidisciplinary Science, Beihang University, Beijing 100191, China.

[e] Key Laboratory of Bio-inspired Smart Interfacial Science and Technology of Ministry of Education, School of Chemistry, Beihang University, Beijing100191, China.

[f] Key Laboratory of Bio-inspired Materials and Interfacial Science, Technical Institute of Physics and Chemistry, Chinese Academy of Sciences, Beijing 100190, China.

E-mail: ypchen0727@buaa.edu.cn, jiangxy@buaa.edu.cn.

View Article Online
DOI: 10.1039/D5MH01249J





**Abstract**

Biological olfactory perception relies on ionic transport, offering a promising alternative to conventional gas sensors that depend on electronic signal transmission, which often suffer from limitations such as limited sensitivity, high power consumption, and susceptibility to moisture. Inspired by biological olfactory ion channels, nanochannel-based ionic membranes incorporating 2D materials and ionic liquids have been developed. Through functional modifications, these membranes exhibit unique tremella-like structures that optimize gas diffusion pathways and provide effective gas interaction sites. The developed membranes demonstrate exceptional performance, including a low detection limit of 189 ppb, a remarkable sensitivity of 2.02%/ppm across 5-500 ppm, specific selectivity to ethanol, stable reversibility over 100 cycles, and ultralow power consumption of only 0.28 μW. Experimental and simulation results confirm that the enhanced sensing performance stems from solvated ion transport within nanoconfined channels. Notably, the membranes maintain detection efficiency under varying humidity conditions, demonstrating practical applicability in both food quality assessment (30-40% RH) and intoxicated driving monitoring (80-90% RH). It is envisioned that the deepened understanding of solvated ion transport within nanoconfined channels will advance the development of bioinspired olfactory perception and integrated sensing systems.

## Introduction

Ion channels in living organisms are characterized by efficient energy consumption, rapid transport, and specific molecular recognition,[1-3] generating significant interest in developing artificial counterparts for various applications,[4, 5] including highly efficient energy harvesting,[6, 7] fine ion/molecule separation,[8] and neuromorphic sensing.[4, 9, 10] In the human olfactory perception system, the interaction between target analytes and human olfactory receptors (HORs) initiates an inward flow of cations ($Na^+$ and $Ca^{2+}$), which opens anion channels and facilitates the transmission of action potentials (Figure 1a).[11] This signal then propagates along neuron axons, traversing from the olfactory bulb through the olfactory tract to the cerebral cortex, ultimately enabling the identification of odor molecules.[12, 13] In response to the limitations of traditional electronic signal-based sensing materials, such as restricted sensitivity, high power consumption, and incompatibility with wet conditions,[14-18] artificial ionic channels that react to physical and chemical stimuli have gained considerable attention. For instance, green alga-inspired nanofluidic heterogeneous membranes were constructed for underwater visual perception by forming an intramembrane electric field.[19] Additionally, a nanofluidic diode, capable of reversibly responding to $CO_2$ in KCl solution, has been developed using

functionally modified conical nanochannels.[9] However, challenges such as limited portability and relatively high mass transfer resistance between the gas and liquid phase may arise due to the fluidic media and high resistance of aqueous media. Despite these challenges, there is potential to create highly sensitive and energy-efficient gas sensing materials based on ionic channels.

Ionic liquids (ILs) possess numerous exceptional features, including low vapor pressure, remarkable chemical and thermal stability, a wide electrochemical window, high ionic conductivity, acceptable biocompatibility, and customizable ionic properties.[20] Moreover, ILs demonstrate a broad range of complex interactions with diverse materials, acting as both gas recognition sites and signal transmission carriers.[4] These interactions between volatile organic compounds (VOCs) and ILs enhance ionic diffusion, creating new opportunities for gas sensing.[4, 21] Taking advantage of these properties, ILs are considered ideal alternatives to inorganic salt ions in artificial gas-sensitive materials, such as ion gels and hydrogels.[22-24] Nanoconfined ILs address key challenges associated with traditional nanofluidic membranes that rely on inorganic electrolytes or bulk ILs, such as encapsulation difficulties, leakage issues, and limited portability.[4] Importantly, nanoconfinement eliminates the need for an aqueous medium, significantly reducing gas diffusion resistance. By strategically selecting the framework materials and ILs, consecutive and layered ion channels have been designed for selective and rapid gas separation.[25-27] Consequently, it is anticipated that nanoconfined ILs could enable highly selective olfactory sensing by converting gas stimuli into detectable ionic signals.[28-30]

In this work, inspired by the human olfactory system, we have developed a tremella-like structured membranes that utilize rapid ion transport in nanochannels and interactions between VOCs and ILs, enabling effective VOC sensing (Figure 1b). Specifically, amino-group-modified graphene oxide (GO) nanosheets act as the framework materials, while ILs confined between the layers function as both gas recognition sites and communication carriers for signal transmission. The incorporation of amino groups plays a crucial role in enhancing the overall performance. By varying the amount of modifier, nanochannel-based ionic membranes can be transformed from compact layered structures to more loosely arranged tremella-like architectures, thereby increasing gas transfer pathways. Consequently, the developed membranes exhibit extraordinary VOC detection capabilities due to the formation of solvated ions within nanochannels, as confirmed by experimental and simulation results. Notably, the tremella-like membranes demonstrate an impressively low LOD of 189 ppb for ethanol. Over a broad concentration range of 5 to 500 ppm, the membranes display a strong linear correlation

between response and ethanol concentration, achieving a remarkable sensitivity of 2.02%/ppm. Even after 100 ventilation cycles, the response of the nanochannel-based ionic membranes remains stable, highlighting their exceptional stability as gas sensing materials. Furthermore, the membranes exhibit specific selectivity for ethanol among other common VOCs due to non-covalent interactions. This outstanding sensing performance makes them well-suited for applications in food quality assessment and drunk driving monitoring, enabling accurate gas detection even under moderate to high humidity conditions, such as assessing strawberry spoilage and monitoring driver alcohol levels.





## Results and Discussion

### Construction of Hierarchical Tremella-like Ionic Membranes

To establish effective pathways for gas transfer and channels for ion transport, membranes of amino-functionalized GO with confined ILs (referred to as $NH_2$-GO/ILs) were prepared (Figure 1c). The pristine GO membranes (GMs) exhibited wrinkled surfaces and clearly defined layered structures (Figure S1a, b), with abundant oxygen-containing groups in GO nanosheets facilitating easy functionalization.[31] Following modification with (3-aminopropyl) trimethoxysilane (APTMS), the $NH_2$-GO nanosheets began to curl, resulting in a more pronounced wrinkled morphology (Figure S2). The introduction of ILs into GMs produced shorter and denser wrinkles within the GO/ILs (Figure S1c), while the visibility of the layered structure diminished due to IL filling (Figure S1d). In contrast, the $NH_2$-GO/ILs displayed uniform and fluffy structures (Figure 1d), with hierarchical pore structure consisting of macropores (marked by white arrows at the bottom and left in Figure 1d) and nanochannels within nanosheets. The edges of the nanosheets appeared smooth and swollen, featuring wider wrinkles on their surfaces, resembling soaked tremella (as indicated by as yellow arrows at the bottom and right in Figure 1d). The thickness of GO/ILs increased to ~ 4.33 μm compared to the 1.45 μm measured for the GMs (Figure S3a, b), which is attributed to the infiltration of ILs within the GO nanosheets. The thickness of $NH_2$-GO/ILs (~ 21.23 μm) exhibited only a modest increase in comparison to that of $NH_2$-GO (~ 17.90 μm, Figure S3c, d), potentially due to the presence of macropores resulting from the curled structure. Energy dispersive X-ray spectroscopy (EDS) mapping confirmed the uniform distribution of elements derived from APTMS (Si) and [BMIM][$NTf_2$] (S and F), thereby indicating successful amino-functionalization and the homogeneous incorporation of ILs into the membranes (Figure 1e).

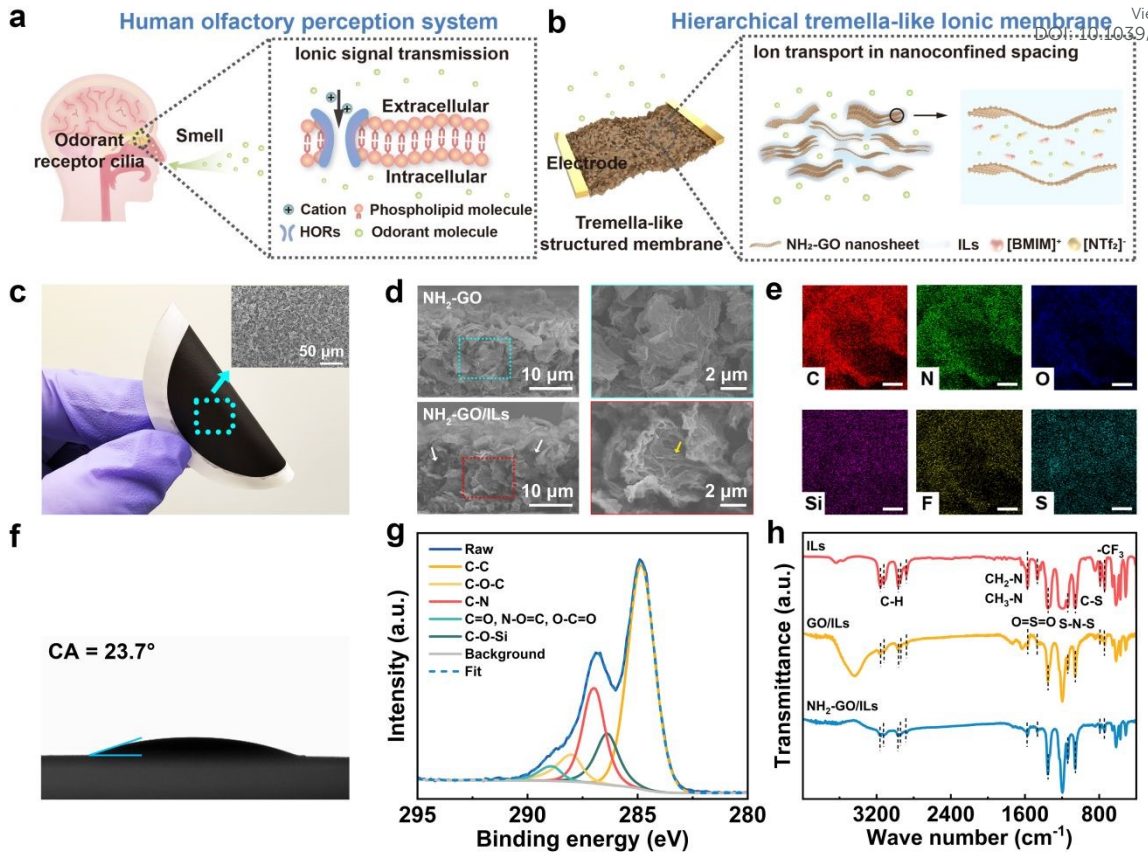


**Figure 1.** (a-b) Bioinspired design of tremella-like ionic membranes for olfactory sensing. (a) Schematic illustration of human olfactory perception: Target analytes reach the HORs on odorant receptor cilia (left), triggering signal transmission through the inward flow of extracellular cations (right). (b) Schematic illustration of bioinspired ionic membranes based on ion transport in nanoconfined spacing (left), with hierarchical pore structure consisting of macropores and nanochannels. $NH_2$-GO nanosheets form nanochannels with confined ILs, which provide gas recognition sites and act as communication carriers (right). (c-h) Construction of nanochannel-based ionic membranes. (c) Digital photograph of the $NH_2$-GO/ILs. The inset is the SEM image of the $NH_2$-GO/ILs. (d) Cross-sectional SEM images and enlarged images of $NH_2$-GO nanosheets before (top) and after (bottom) introducing ILs. White arrows in the left image denote the appearance of voids in $NH_2$-GO/ILs, and yellow arrows in right images represent wrinkles observed in membranes. (e) EDS mapping of $NH_2$-GO/ILs, the scale bar represents 2 μm. (f) Contact angle of [BMIM][$NTf_2$] on $NH_2$-GO nanosheets. (g) XPS spectrum of $NH_2$-GO nanosheets. (h) FTIR spectra of ILs, GO/ILs, and $NH_2$-GO/ILs.

The contact angle (CA) test results for ILs on $NH_2$-GO nanosheets were measured to be 23.7°, indicating that the nanosheets exhibit a strong affinity for ILs (Figure 1f). This finding confirms the presence of capillary forces, which facilitate the effective infiltration of ILs into the

View Article Online
DOI: 10.1039/D5MH01249J

nanospace within nanosheets. To further demonstrate the presence of ILs within the nanosheets, a control experiment was conducted by dropping equal weights of ILs onto the surface of $NH_2$-GO membranes. The cross-sectional morphology of the membranes, treated with and without vacuum filtration, was subsequently compared (Figure S4). The results revealed that ILs were almost absent in the inner macropores of the vacuum-filtered membranes (Figure S4a, b), while the macropores of the membranes without vacuum filtration were entirely filled with ILs (Figure S4c, d). This observation indicates that the $NH_2$-GO/ILs membranes are not merely filled with ILs within the macropores; rather, the ILs are confined to the interlayers of the nanosheets and their surfaces. The ILs on the surface of the nanosheets play a crucial role in facilitating ion transport across adjacent nanosheets, while the ILs confined within the interlayers are vital for gas sensing.

Spectroscopic characterization techniques, including X-ray photoelectron spectroscopy (XPS) and Fourier transform infrared (FTIR) spectroscopy, were employed to analyze the chemical structures of nanosheets before and after functional group modification. The XPS spectra of GO and $NH_2$-GO nanosheets displayed the presence of C-N, N-O=C, and C-O-Si bands, confirming the successful attachment of APTMS to GO nanosheets (Figure S5 and Figure 1g). In the FTIR spectrum of GO, characteristic bands at 1726 $cm^{-1}$, 1630 $cm^{-1}$, and 3427 $cm^{-1}$ denote C=O, C=C, and -OH functionalities, respectively (Figure S6). For $NH_2$-GO, the emergence of peaks at 1073, 1226, and 2926 $cm^{-1}$ is attributed to Si-O-Si, C-Si, and -$CH_2$ moieties introduced by APTMS. Additionally, a broad band at 1407 $cm^{-1}$ corresponds to the C-N stretching vibration. Notably, the redshift of C=O stretching to 1707 $cm^{-1}$ is attributed to nucleophilic substitution reactions with amino groups from APTMS.[32] These FTIR results validate the successful functionalization of GO nanosheets via reactions with the oxygen-containing groups.

The introduction of ILs within nanosheets results in increased interlayer spacing and the formation of intermolecular interactions between ILs and the nanosheets. X-ray diffraction (XRD) analysis revealed an increase in *d*-spacing for GO/ILs from 0.71 to 1.99 nm (Figure S7). For $NH_2$-GO, the (001) peaks in the XRD spectra become weaker and less pronounced with the addition of APTMS due to the reduced regularity (Figure S8). FTIR spectra confirmed the successful integration of [BMIM][$NTf_2$] with both GO and $NH_2$-GO nanosheets (Figure 1h), as evidenced by the presence of characteristic peaks of ILs in both GO/ILs and $NH_2$-GO/ILs. Discernible shifts in these characteristic peaks (Table S1) indicate interactions between ILs and the nanosheets. Specifically, the most significant shifts were observed in GO/ILs for cation-related vibrations: the imidazole ring C-H stretching vibration peak at 3162.41 $cm^{-1}$, the N-Bu,

N-Me stretching vibration peak at 1196.83 $cm^{-1}$, and the C4-H and C5-H in-plane rocking vibration peaks at 837.65 $cm^{-1}$. Similar shifts occurred in $NH_2$-GO/ILs at 3155.41, 3120.11, 1196.58, and 838.25 $cm^{-1}$. Furthermore, $NH_2$-GO/ILs exhibited increased peak shifts for C2-H, O=S=O, and C-S stretching vibrations. This enhancement arises from stronger dipole-dipole interactions between the polar IL components and $NH_2$-GO, where the exposed amine groups elevate local polarity. These results indicate the existence of interactions such as electrostatic interactions, π-π interactions, and hydrogen bonding between the nanosheets and ILs.[33] Notably, anion peak shifts were relatively subtle compared to the pronounced cation shifts. This observation highlights the greater affinity of IL cations for the negatively charged nanosheets (Figure S9), primarily driven by electrostatic interactions. This preferential cation affinity leads to the arrangement of IL cations along the nanosheet surface, forming ordered interfacial layers that minimize repulsion between adjacent cations while facilitating directional ion migration.

These findings underscore the successful development of hierarchical tremella-like ionic membranes, characterized by gas-permeable macropores and localized ion-rich channels. The unique tremella-like structures of the sensing membranes provide abundant pathways for gas transfer. Furthermore, the significant interactions between nanosheets and cations strengthen the nanoconfinement effect, establishing an optimal platform for bioinspired olfactory sensing.

**Olfactory Sensing Performance**

To evaluate the advantages of nanochannel-based ionic membranes for olfactory sensing, the sensing performance of bulk ILs was initially assessed. The results showed only slight signal fluctuations attributed to the fluidic properties of ILs when subjected to a constant $N_2$ flow of 1000 mL/min (Figure S10a). Upon exposure to 100 ppm ethanol, the fluctuations intensified; however, the gas response was obscured by these fluctuations (Figure S10b). This finding indicates that the high viscosity of ILs imposes challenges on gas diffusion, thereby hindering the sensing process.[34] Moreover, a substantial portion of ILs exists as cation-anion aggregates. Even when localized ion dissociation occurs in the presence of VOCs, the overall change in ionic conductivity remains minimal (Figure S10c, d).

The IL content within the membranes was optimized by adjusting the feeding ratios ($m_{ILs}/m_{GO}$ or $m_{ILs}/m_{NH_2\text{-}GO}$) during membrane preparation (Figure S11a, b). An increase in IL content enhanced the gas response; however, the gas response decreased when the feeding ratios exceeded 800 for ethanol, regardless of whether using GO/ILs or $NH_2$-GO/ILs. Higher IL content improved the availability of gas-combining sites, but excessive amounts compromised gas permeability due to bulk characteristics. Consequently, a feeding ratio of 800 was selected

View Article Online
DOI: 10.1039/D5MH01249J

for further testing to ensure an optimal gas sensing response, which results in an $NH_2$-GO/ILs membrane containing 87.81 wt% ILs. The initial amount of nanosheets also influences gas sensing performance. The ethanol response increases as the weight of $NH_2$-GO increases from 2.5 to 5.0 mg, but decreases with further addition of nanosheets (Figure S11c). It is suggested that inadequate nanosheets do not facilitate effective conductive pathway formation, while an excess of nanosheets extends extra gas diffusion pathways, hindering gas sensing. Furthermore, modifications with APTMS significantly altered the morphologies of the ionic membranes (Figure S12a-e). As APTMS content increased, the membrane surface transitioned from dense to rough, and voids appeared when the added APTMS content exceeded 50 wt%, leading to nanosheet agglomeration (Figure S12a-e, and S13). The gas sensing response of $NH_2$-GO/ILs membranes indicated that the optimal response occurred at 50 wt% APTMS due to the established gas transfer pathways, while insufficient or excessive modification reduced the efficiency of these pathways (Figure S12f).

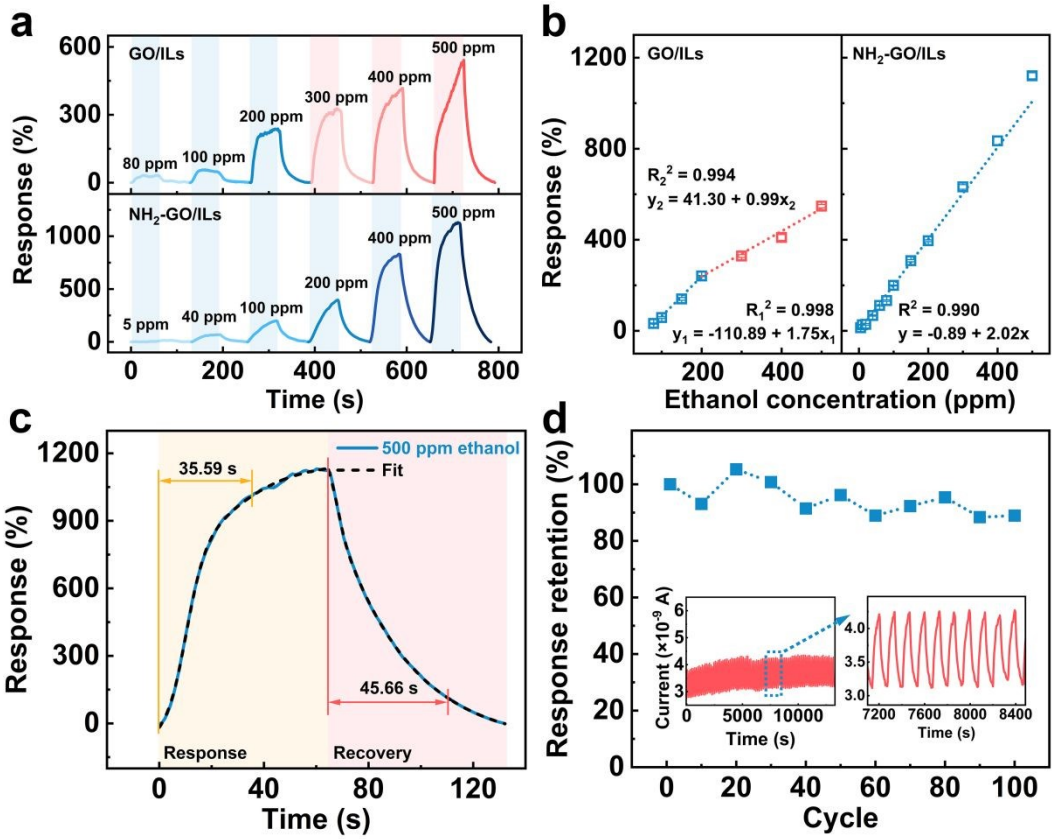


**Figure 2.** Ethanol sensing performance of the prepared membranes based on GO/ILs and $NH_2$-GO/ILs. (a) Dynamic response curves of GO/ILs and $NH_2$-GO/ILs. (b) Response of GO/ILs and $NH_2$-GO/ILs to ethanol with different concentrations. (c) Response and recovery time of $NH_2$-GO/ILs to 500 ppm ethanol. (d) Cyclic sensing response of $NH_2$-GO/ILs to 20 ppm ethanol. The insets show the original *I-t* curve and its partially magnified curve.

View Article Online
DOI: 10.1039/D5MH01249J

The sensing performance of the $NH_2$-GO/ILs was rigorously evaluated under optimized conditions. *I-t* curves were recorded at a constant voltage, allowing for the calculation of the response according to equation (1):

$$Response\ (\%) = \frac{\Delta I}{I_0} \quad (1)$$

Where $I_0$ and $\Delta I$ denote the baseline current under pure $N_2$ flow and the current variation upon exposure to target gases, respectively. As shown in Figure 2a, the $NH_2$-GO/ILs exhibited a positive response to varying ethanol concentrations at room temperature. Sensitivity was determined from the linear correlation between response and ethanol concentration, defined as the change in current per unit concentration and represented by the slope of the line fitted to the data. In pristine GO/ILs, the response increased from 32.23% to 547.79% as ethanol concentrations increased from 80 to 500 ppm (Figure 2b), exhibiting two distinct linear regions: a high sensitivity of 1.75%/ppm ($R_1^2$ = 0.998) below 200 ppm, and a reduced sensitivity of 0.99%/ppm ($R_2^2$ = 0.994) beyond this threshold. This decrease in sensitivity originates from the limited gas transfer pathways in compactly stacked GO layers, leading to large diffusion resistance and incomplete site accessibility. In contrast, the $NH_2$-GO/ILs exhibited an impressive linear response range of 13.23% to 1120.37% over 5 to 500 ppm, with a sensitivity of 2.02%/ppm ($R^2$ = 0.990). Amino-functionalization engineered hierarchical porosity and established gas diffusion pathways, thereby eliminating mass transport limitations. This structural optimization enables ethanol molecules to access adsorption sites proportionally across the wide concentration range, avoiding saturation effects. The theoretical LOD of $NH_2$-GO/ILs was calculated as only 188.99 ppb (for calculation details, see the Supporting Information and Table S2). Furthermore, the response time ($\tau_{res}$, i.e., the time required to reach 90% of the equilibrium response) and the recovery time ($\tau_{rec}$, i.e., the time required to recover 90% of the equilibrium response) were recorded as 35.59 s and 45.66 s, respectively, for exposure to 500 ppm ethanol (Figure 2c). Over 100 cycles of response and recovery at 20 ppm ethanol, the response of $NH_2$-GO/ILs exhibited slight fluctuations but remained at 88.92% (Figure 2d), affirming their reliability. The power consumption during the single response-recovery process was notably low at 0.284 μW (Figure S14). In addition, the hierarchical tremella-like ionic membranes in this work demonstrate competitive performance among recent ethanol sensors based on electronic signal transmission, featuring an extremely low LOD of 0.19 ppm, high sensitivity of 2.02%/ppm across a wide linear range of 5-500 ppm (for comparison references, see Supporting Information and Table S3), highlighting their excellent potential for practical applications.

View Article Online
DOI: 10.1039/D5MH01249J

## Potential Sensing Mechanism

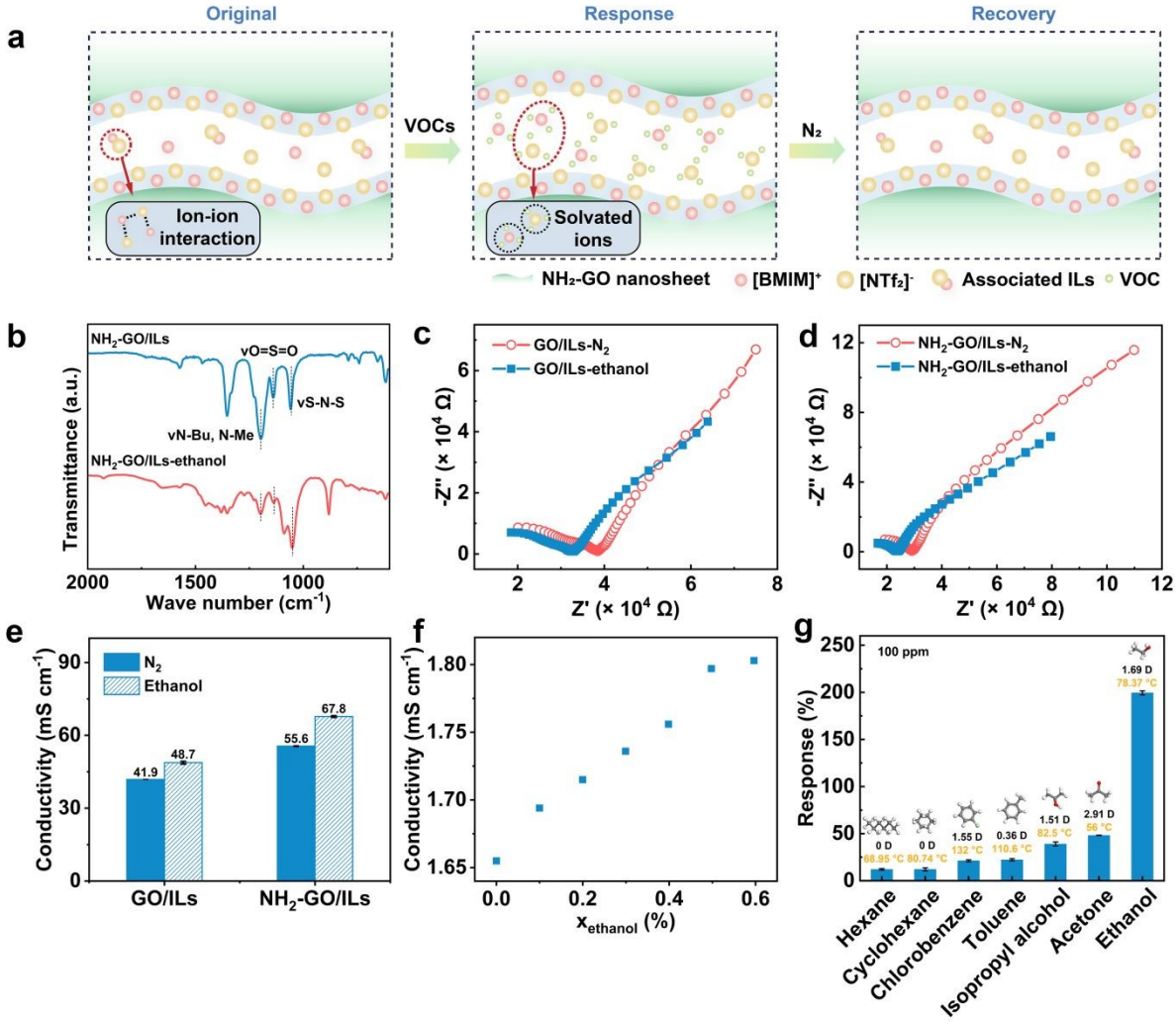


**Figure 3.** Potential sensing mechanism. (a) Schematic illustration of the potential sensing mechanism of the nanochannel-based ionic membranes. (b) FTIR spectra of $NH_2$-GO/ILs before and after treatment with ethanol. (c, d) Nyquist plots of (c) GO/ILs and (d) $NH_2$-GO/ILs without and with ethanol treatment. (e) Ionic conductivity of GO/ILs and $NH_2$-GO/ILs with $N_2$ and ethanol treatment calculated from EIS results. (f) The conductivity of [BMIM][$NTf_2$]-ethanol mixture with the addition of ethanol. The abscissa is volume fraction of ethanol. (g) Response of $NH_2$-GO/ILs membranes to various VOCs with a concentration of 100 ppm.

The potential sensing mechanism of the nanochannel-based ionic membranes is depicted in Figure 3a. Initially, ILs exhibit relatively high viscosity due to electrostatic interactions among the ions (Figure 3a, left), which hinder ion diffusion and diminish conductivity. In the initial stage, gas molecules diffuse into the macropores of the hierarchical membranes. Subsequently, they penetrate the nanoconfined channels to interact with cations and anions. Through non-covalent interactions, such as hydrogen bonding and dipole-dipole interactions with

[BMIM][$NTf_2$], solvated ions are formed (Figure 3a, middle).[35] After purging $N_2$, the nanoconfined spaces restore the original ionic state dominated by weak non-covalent interactions, which driven by thermodynamic equilibration and nanoconfined ion reorganization (Figure 3a right). These interactions can be verified by shifts in the FTIR spectra at critical vibrational peaks, including N-Bu and N-Me stretching at 1196.60 $cm^{-1}$, O=S=O stretching at 1352.61 $cm^{-1}$, and S-N-S stretching at 1058.18 $cm^{-1}$ (Figure 3b, Table S4). The formation of solvated ions significantly influences both ionic diffusion and conductivity.[36] The viscosity of the IL-VOC mixture ($\eta$) can be expressed using Seddon's equation:[37]

$$\eta = \eta_S \exp\left(-\frac{\chi_{CS}}{a}\right) \quad (2)$$

Where $\eta_S$ represents the viscosity of pristine [BMIM][$NTf_2$]. $\chi_{CS}$ denotes the molar fraction of the VOC, while $a$ signifies a specific IL constant. The relationship between diffusion coefficient ($D$) and $\eta$ is described by the Stokes-Einstein equation:[38]

$$D = \frac{\kappa_B T}{6\pi\eta r} \quad (3)$$

In this equation, $\kappa_B$ is the Boltzmann constant, $T$ stands for absolute temperature, and $r$ is the effective ionic radius. As gas molecules permeate the ion channels and interact with the cations and anions, the electrostatic interactions weaken, resulting in reduced viscosity and enhanced ionic diffusion, which in turn increases ionic conductivity.[39, 40] When the gas concentration increases, the probability of gas molecules contacting ionic active sites increases. This intensifies ion solvation, which disrupts cation-anion electrostatic interactions and enables ions to overcome spatial constraints imposed by channel walls. The ionic conductivity was determined using electrochemical impedance spectroscopy (EIS). Upon exposure to ethanol, a decrease in impedance was observed (Figure 3c, d), corresponding to a modest increase in ionic conductivity due to enhanced mobility of solvated ions. However, it is critical to distinguish between the steady-state ion transport properties measured by EIS[41] and the dynamic interfacial processes governing the current response in *I-t* curves. Under a constant direct current, gas sensing performance is dominated by transient phenomena such as concentration polarization, charge transfer resistance, and field-driven ion migration kinetics.[41, 42] These processes are undetected by EIS, which probes equilibrium bulk conductivity through small-amplitude alternating current bias. *I-t* measurements exhibit significantly higher sensitivity to gas-surface interactions, capturing kinetic ion migration effects rather than steady-state conductivity. To further substantiate the enhanced conductivity, small amounts of ethanol were gradually added to the ILs, and the conductivity of mixture was measured. Conductivity surged from 1.66 to 1.80 mS $cm^{-1}$ (Figure 3f), confirming the proportional relationship between ionic mobility and

View Article Online
DOI: 10.1039/D5MH01249J

ethanol content (Figure 3f). Therefore, the VOC sensing mechanism in nanoconfined IL membranes is attributed to the enhanced diffusion of solvated ions under weak interactions, which results in an increase in current.

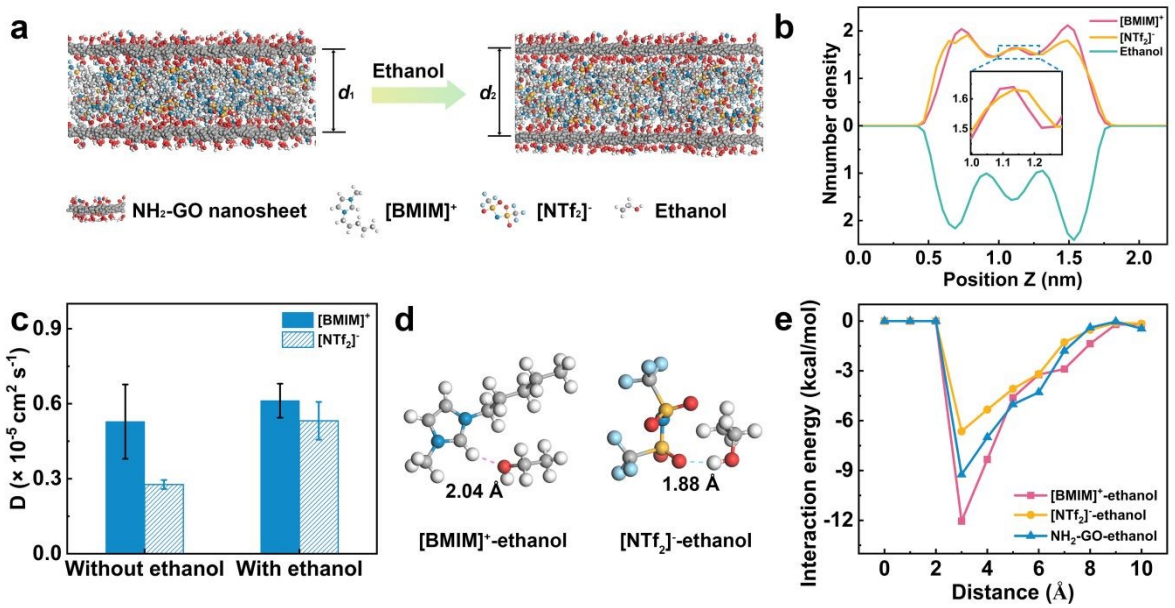


**Figure 4.** (a) Molecular structures of ILs confined in the $NH_2$-GO nanochannels (left) and treated with ethanol (right). (b) Spatial distribution of the centers of mass of $[BMIM]^+$, $[NTf_2]^-$, and ethanol along the vertical direction within the $NH_2$-GO nanoconfined channel. The inset is the partially enlarged plots. (c) Diffusion coefficient ($D$) of $[BMIM]^+$ and $[NTf_2]^-$ without and with ethanol treatment, which was obtained from the slopes of MSD versus time. (d) Optimized structures of the most stable interaction modes for $[BMIM]^+$-ethanol and $[NTf_2]^-$-ethanol. (e) Interaction energy between ethanol and ILs confined in the GO nanochannel, measured from simulation data as functions of $[BMIM]^+$-ethanol, $[NTf_2]^-$-ethanol, and $NH_2$-GO-ethanol distances.

To verify the exceptional selectivity of bioinspired ionic membranes for ethanol, the sensing performance of other VOCs with varying polarity and boiling points was assessed (Figure 3g). Research indicates that increased polarity and decreased boiling point of VOCs enhance their interactions with ILs, such as dipole-dipole interaction.[23] Among nonpolar VOCs, hexane and cyclohexane exhibited the lowest response, at 12.06% and 12.08%, respectively. Chlorobenzene and toluene showed similar responses of 21.20% and 22.22%, respectively; chlorobenzene is relatively polar (1.55 D), and toluene has a lower boiling point of 110.8 °C. Notably, isopropyl alcohol, despite its similar polarity to chlorobenzene, exhibited a higher response of 38.98% due to its much lower boiling point (82.5 °C). The highest selectivity for

View Article Online
DOI: 10.1039/D5MH01249J

ethanol is attributed to its weaker α-C-H bond compared to secondary alcohols like isopropyl alcohol, leading to more stable hydrogen bonding with the sensing materials.[43] The response of the nanochannel-based ionic membranes to ethanol was the highest among the tested VOCs. FTIR spectroscopy further characterized the interactions between four representative VOCs (ethanol, acetone, toluene, and hexane) and $NH_2$-GO/ILs as well as $NH_2$-GO nanosheets (Figure S14, Figure S15). Among the examined VOCs, ethanol produced the most significant peak shifts related to ILs (Figure S15, Table S5), reflecting a strong affinity between ethanol and the tremella-like structured membranes. Only minor spectral shifts were observed for other VOCs, suggesting weaker solvation effects. The interactions of VOCs with $NH_2$-GO nanosheets were also investigated (Figure S16, Table S6), revealing notable peak shifts for ethanol and toluene. For ethanol, the O-H stretching vibration blue-shifted by 2.16 $cm^{-1}$ due to hydrogen bonding with $NH_2$-GO nanosheets. For toluene, the C-H stretching vibration on the aromatic ring at 2880.34 $cm^{-1}$, along with out-of-plane C-H deformation peak at 1859.96 $cm^{-1}$, and the $CH_3$ bending vibration at 1459.52 $cm^{-1}$, shifted by 1.51, 1.57, and 1.21 $cm^{-1}$, respectively, likely due to π-π interaction with nanosheets. The hydrogen bonding between nanosheets and ethanol enhances the permeability of ethanol into nanochannels, facilitating interactions with confined ILs.[44] Thus, the extraordinary selectivity of nanoconfined ion channel membranes for ethanol can be attributed to dipole-dipole interactions between ethanol and ILs, as well as hydrogen bonding among ethanol, ILs, and amino-functionalized nanosheets.

To elucidate the solvated gas sensing mechanism within nanochannels, molecular dynamics (MD) simulations were conducted to study the structures of the ionic nanochannel and the dynamics of the system. The *d*-spacing of nanoconfined ion channels before ($d_1$) and after introducing ethanol ($d_2$) were predetermined according to experimental results. The vertical distribution of ions shows distinct layered architectures (Figure 4a left and S17), with the primary peaks of $[BMIM]^+$ and $[NTf_2]^-$ positioned near the channel walls, displaying a noticeable shift. The high density of $[BMIM]^+$ near the channel walls is attributed to the negatively charged nanosheets. Upon introducing ethanol, the mass distribution centers of ethanol overlap with the high-density regions of both cations and anions, indicating the strong affinity between ethanol and ILs (Figure 4a right and b). Simultaneously, the peaks for $[BMIM]^+$ and $[NTf_2]^-$ in the central region shift noticeably, indicating the formation of solvated ions, which facilitates ion dissociation (Figure 4b).[45] To evaluate ion diffusion coefficients, ion mean square displacement (MSD) curves versus time were simulated (Figure S18). The results indicate 15.09% and 89.29% increase in *D* of $[BMIM]^+$ and $[NTf_2]^-$ in the presence of ethanol, with the increase being more pronounced for anions (Figure 4c). This difference is attributed to

View Article Online
DOI: 10.1039/D5MH01249J

the fact that cations are more constrained due to the stronger electrostatic attraction to the negatively charged channel walls. The formation of solvated ions involves a dynamic arrangement in which ethanol molecules interact with the ions through electrostatic forces, hydrogen bonding, and van der Waals interactions. The optimized molecular configuration is shown in Figure 4d. The polar hydroxyl group of ethanol engages in hydrogen bonding and dipole interactions with the cation. For imidazolium-based cations, the acidic C2-H proton interacts with the oxygen lone pairs of ethanol, with an interaction distance of 2.04 Å. The anions, characterized by a delocalized negative charge, act as a hydrogen bonding acceptor for the hydroxyl group of ethanol. The interaction distance between the anion and ethanol (~1.88 Å) is shorter due to the strong electronegativity and flexible configuration. Ethanol molecules preferentially cluster around the charged regions of the ions (e.g., the imidazolium ring of $[BMIM]^+$ and $[NTf_2]^-$). As a result, a dynamic solvation shell forms as ethanol molecules surround cations and anions. The interaction energy calculated from MD simulations shows that ethanol binds more strongly to $[BMIM]^+$ than to $[NTf_2]^-$ and nanosheets, primarily due to the localized high charge density regions of the imidazolium ring (Figure 4e). Therefore, the formation of solvated ions reduces the electrostatic interactions between cations and anions, promoting their dissociation and enhancing ion diffusion, in agreement with our experimental results.

**Food Quality Monitoring and Exhaling Alcohol Detection**

In the atmosphere, ubiquitous water vapor competes with gas-sensing materials relying on electronic transmission, presenting challenges for gas detection in humid conditions. To evaluate the effectiveness of bioinspired ionic membranes in such environments, two humidity scenarios were examined: moderate (30-40% RH) and high (80-90% RH), focusing on food quality monitoring and alcohol detection in exhaled breath. Initially, the feasibility of membranes for monitoring strawberry spoilage was explored. Given the susceptibility of strawberries to mechanical damage and fungal infections during storage and transport, spoilage is inevitable. Therefore, establishing a non-destructive method to monitor fruit quality changes is urgently needed to prevent further economic loss. Studies have indicated that various VOCs are released during strawberry spoilage, including 2-methyl propyl ester (28.5%), ethanol (19%), 2-methyl acetate (15.6%), and $CO_2$ (16%).[46, 47] Ethanol, a key VOC biomarker, is particularly important due to its relatively high content. In this study, a batch of fresh *Hongyan* strawberries, characterized by vibrant colors and no visible injuries, was selected and placed in a vacuum dryer at room temperature. Gas emissions from strawberries were collected every 24

h using a diaphragm pump, while the vacuum dryer was replenished with fresh air (Figure 5a). Interestingly, the membranes did not show a distinct response to the characteristic gases emitted by *Hongyan* strawberries but did exhibit a specific response to ethanol at the same concentration of 100 ppm (Figure S19). This high ethanol response laid the groundwork for detecting variations in ethanol concentration within the gas mixture. The dynamic response curves of the ionic membranes to the gases released from the strawberries are presented in Figure 5b. To account for the water vapor emitted during storage, a reference baseline was established using air at 40% RH, which exhibited a response of 250.26% (Figure S20). This humidity-induced response arises from the partial solvation effects between water and ions (Figure S21).[48, 49] The intrinsic humidity sensitivity originates from water-triggered ion solvation and enhanced ion mobility. Crucially, humidity levels during the first five days of ethanol detection remained within 30-40% RH, ensuring that ethanol signals remained decoupled from humidity variations. Strawberries retained their freshness from the first to the second day, with minimal current fluctuations (from 1816.36% to 2122.27%), and a significant increase in response was observed from the third day onward (5894.16%). The decay index, which quantifies spoilage extent, was calculated using statistical methods outlined in the Supporting Information.[50] It has been reported that strawberries lose their commercial value when the decay index reaches 30%.[51] As illustrated in Figure 5c, the color of the strawberries gradually darkened from the first day to the fifth day, with visible mildew appearing by the third day (marked as the yellow circle), coinciding with an increase in the decay index to 41.67%. This increase correlates with the rising response, indicating a loss of commercial value. Overall, these results suggest that nanochannel-based ionic membranes can effectively monitor strawberry spoilage at room temperature. This method provides a viable approach for assessing food freshness and ensuring food quality and safety.

Exhaled gas contains significant water vapor, which complicates the detection of its components, particularly in high-humidity conditions. In China, a blood alcohol concentration (BAC) exceeding 20 mg/100 mL is illegal for driving, while a BAC above 80 mg/100 mL classifies as driving while intoxicated, potentially resulting in criminal charges. To evaluate the ethanol sensing capability of the developed membranes, their response was compared to BAC measurements recorded by a commercial breathalyzer (Figure 5d). The initial exhaled gas, collected before drinking, served as a reference and exhibited a humidity of 90% RH with a response of 1328.73% (Figure S22). This response is attributed to partial solvation induced by water molecules, which could be further amplified by subsequent interaction with ethanol molecules. The start of alcohol consumption was recorded as 0 h, and exhaled gases were

View Article Online
DOI: 10.1039/D5MH01249J

collected every 2 h. Over time, ethanol was metabolized in the body, resulting in a gradual decrease in BAC (Figure S23), which was reflected by the decreasing sensing response of the membranes. After 8 h, the response returned to baseline levels, indicating near-complete alcohol metabolism (Figure 5e). A linear correlation was observed between the sensing response and BAC in the 2-8 h range (Figure 5f). The variation at 0 h likely stems from the excessively high alcohol concentration. It suggests that even in high-humidity scenarios, the interaction between target gases and partially solvated ions remains selective and concentration-dependent. According to the fitted equation, a response below 3658.06% indicates no alcohol, while a response exceeding this threshold indicates drunk driving. Additionally, a response surpassing 9632.86% signals driving while intoxicated. These results highlight the capability of the developed membranes to detect ethanol even under high-humidity conditions.

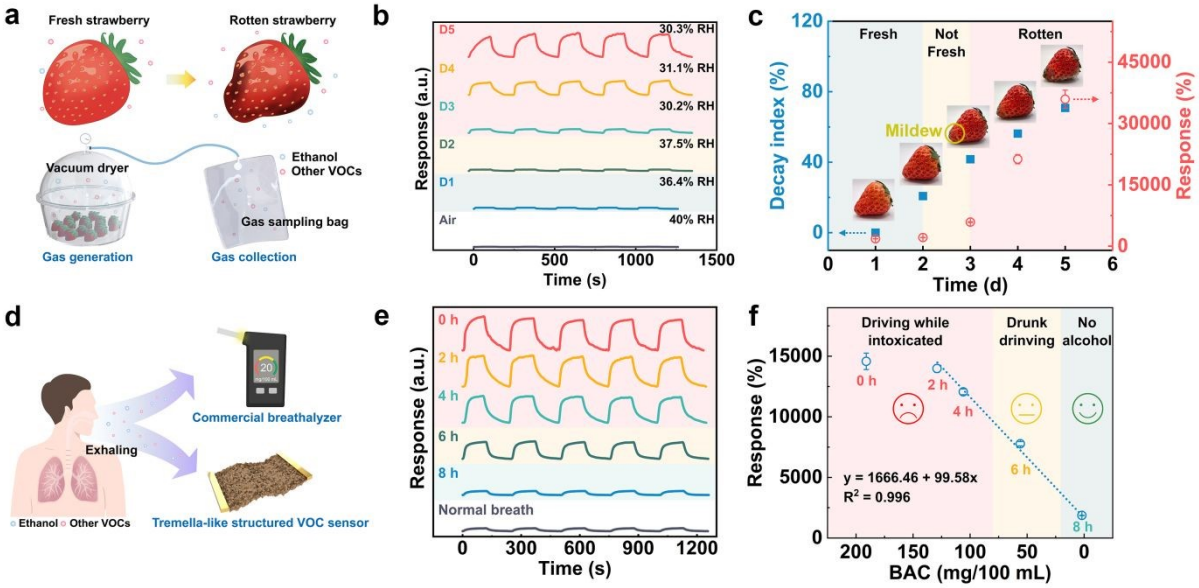


**Figure 5.** Wet ethanol sensing performance of the hierarchical tremella-like ionic membranes for food quality monitoring and exhaling alcohol detection. (a) Schematic illustration of strawberry spoilage and the gas collection process. (b) The dynamic response curves of membranes to air with 40% RH and gases released by strawberries. (c) The decay index of strawberries and the response of the nanochannel-based ionic membranes increased with time. The insets are the digital photographs of strawberries on varying days. (d) Schematic illustration of the exhaling alcohol detection by commercial breathalyzer and the fabricated membranes. (e) The dynamic response curves of the membranes to exhaled gases with and without drinking. (f) The linear correlation between the response of the membranes and the BAC of commercial breathalyzer from 2-8 h (fitting equation: $y = 1666.46 + 99.58x$, $R^2 = 0.996$).

View Article Online
DOI: 10.1039/D5MH01249J





## Conclusion

In conclusion, inspired by the human olfactory system, a novel hierarchical tremella-like ionic membrane based on solvated ion transport in nanoconfined ion channels has been successfully developed. The incorporation of ILs within the interlayer spacing of $NH_2$-GO nanosheet-assembled membranes provides gas recognition sites and facilitates efficient signal transport. The membranes exhibit distinctive tremella-like morphologies with increased specific surface areas, enhancing gas transfer pathways and enabling effective interaction with VOCs. Leveraging the solvated ion transport mechanism, the developed membranes demonstrate an impressively low LOD of 189 ppb and a high sensitivity of 2.02%/ppm within the concentration range of 5 to 500 ppm, along with ultralow power consumption of 0.28 μW for a single response process. Moreover, the membranes exhibit specific selectivity for ethanol and excellent reversibility over 100 cycles, highlighting their suitability for applications in two typical humid environments: food quality evaluation and intoxicated driving monitoring. It is anticipated that by further tuning the properties of ILs and the wettability of framework materials, effective gas sensing in extremely high humidity or even underwater conditions can be realized to contribute to developing high-level integrated sensing systems.

## Experimental

*Materials:* Graphene oxide (GO, XF002-3) was obtained from Xianfeng Nanomaterials Technology Co., Ltd, China. 1-butyl-3-methylimidazolium bis[(trifluoromethyl)sulfonyl]imide ([BMIM][$NTf_2$]) was supplied by Lanzhou Yulu Fine Chemical Co., Ltd, China. Hexane (> 99%), cyclohexane (AR, 99.5%), chlorobenzene (AR, 99%), toluene (≥ 99.5%), isopropyl alcohol (> 99%), acetone (≥ 99.5%), ethanol (99.7%), (3-Aminopropyl) trimethoxysilane (APTMS, 97%), 2-ethylhexyl acetate (2-EA, 99%), 2-methylbutyl acetate (2-MA, 99%), ethyl butyrate (EB, 99%), ethyl hexanoate (EH, 99%), and propyl isobutyrate (PI, ≥ 97%) were purchased from Aladdin Reagent Co. Ltd., Shanghai, China. Polyvinylidene fluoride membrane (47 mm, 0.1 μm, hydrophilic) was bought from Nantong Longjin Membrane Technology Co., Ltd. Liquor (alcohol content of 52 vol%) and *Hongyan* strawberries were bought from the local supermarket. The commercial breathalyzer (RD930) was acquired from Shenzhen Red Dragon Instruments Co., Ltd.

*Modification of $NH_2$-GO Nanosheets:* GO powder (100 mg) was dispersed in a mixed solvent containing water and ethanol in a 1:1 volume ratio (50 mL). A homogeneous GO dispersion (2 mg/mL) was obtained by ultrasonic treatment for 1 h. Different mass fractions of APTMS (25 wt%, 50 wt%, 75 wt%, and 100 wt%) relative to the GO weight were added to the above

View Article Online
DOI: 10.1039/D5MH01249J

dispersion. The mixture was then refluxed at 70°C under a $N_2$ atmosphere for 24 h (Figure S24a). The reaction products were meticulously washed with ethanol and water several times to eliminate any unreacted or residual substances. After freezing with liquid nitrogen and subsequent freeze-drying, the modified GO nanosheets with varying degrees of APTMS modification were obtained and denoted as $NH_2$-GO.

*Preparation of Nanoconfined Ionic Membranes:* GO nanosheets (5 mg) were carefully weighed and then dispersed in ethanol (10 mL) using ultrasonic treatment for a duration of 30 min. ILs were subsequently introduced to the GO dispersion at different feeding ratios ($m_{ILs}/m_{GO}$), specifically 200, 400, 600, 800, and 1000. The resulting mixture was subjected to an additional ultrasonication for 30 min, which effectively facilitated the formation of a homogenous GO/ILs dispersion (Figure S24b). A series of GO/ILs membranes with varying IL content were successfully obtained using vacuum filtration on a PVDF filter membrane with a pore size of 100 nm. $NH_2$-GO/ILs membranes were prepared using the same procedure. All membranes were dried at 60 °C for 6 h to eliminate residual ethanol. Before the sensing tests, the samples were additionally dried at 60 °C for 1 h to remove any potentially absorbed molecules.

*Characterization:* The morphologies of nanosheets and the prepared membranes were observed with a field emission scanning electron microscope (FE-SEM, SU8010, Hitachi). The chemical structure of nanosheets was determined by Fourier transform infrared spectroscopy (FTIR, Excalibur 3100, Varian) and X-ray photoelectron spectroscopy (XPS, ESCALAB Xi+, Thermo). The *d*-spacing of membranes was measured by X-ray polycrystalline diffractometer (XRD, D8 focus, Bruker). The Zeta potential of nanosheets was obtained by a Zeta potential analyzer (Nano ZS ZEN3600, Malvern). Electrochemical impedance spectroscopy (EIS) was performed by an electrochemical workstation (CHI-760E, Shanghai Chenhua Instruments Co., Ltd, China). The frequency range for EIS measurements was from $10^5$ to 0.1 Hz.

*Sensing Performance Measurements:* To measure the current change of ion channel-based membranes, gas delivery was facilitated through a dynamic dilution gas mixer (H310V, Huayi). This apparatus effectively diluted gases of high concentrations to the targeted concentration, enabling a cyclic two-step ventilation procedure. In the initial step, only $N_2$ was introduced at a consistent flow rate of 1000 mL/min for 1 min. Subsequently, in the second step, $N_2$ and the targeted high-concentration gas were introduced at varying flow rates while ensuring that the total flow rate remained constant at 1000 mL/min. By precisely adjusting the flow rate ratio between $N_2$ and the VOCs, the output VOC concentration could be effectively regulated. The current was measured using a semiconductor characterization system (4200-SCS, Keithley) with a constant voltage of 5 V. To ensure reliable electrical contact between the probe and the

View Article Online
DOI: 10.1039/D5MH01249J

sample, conductive silver paste was applied to both ends of the sample, and a gold-plated tungsten steel probe (tip diameter of 30 μm) was employed for testing.

*Molecular Dynamics Simulation Details:* Molecular dynamics simulations were performed using the GROMACS software package (version 2021.3).[52, 53] The molecules were first optimized in ORCA, and the $NH_2$-GO was optimized in CP2K. The system was constructed by Packmol.[54] The atomic interactions were parameterized by the optimized potentials for liquid simulations all-atom (OPLS-AA) force field,[55] and a non-bonded force field model with advanced restrained electrostatic potential (RESP2) charge obtained from Multiwfn was applied in the calculations.[56] After the energy minimization, the systems were pre-balanced in the NPT ensemble with the Berendsen method for 5 ns. Then, the production run was carried out in the NPT ensemble at 300 K with the time step of 1 fs. The temperature of the system was controlled by a V-rescale thermostat ($\tau_T$ = 1 ps), and the Parrinello-Rahman pressure coupling was applied to control the pressure. After 20 ns of simulation, the distribution of the particles was analyzed by the toolkits of GROMACS. The diffusion coefficients of cations and anions were calculated according to Einstein's relation. The linear correlation between time ($t$) and the MSD of the dynamical variable yields the corresponding transport coefficient. The interaction energies of ethanol-components ($[BMIM]^+$, $[NTf_2]^-$ and $NH_2$-GO) were calculated as $E = E_{ethanol} + E_{com} - E_{ethanol+com}$. Here, $E_{ethanol}$ is the energy of ethanol in the nanoconfined channel, $E_{com}$ is the energy of the single components in the membrane, and $E_{ethanol+com}$ is the energy of the complex with ethanol binding with components.

## Author Contributions

L. X. and Y. C. conceived the concept. X. J. and L. J. supervised the project. L. X. conducted the experiments and wrote the initial manuscript. H. L., Q. S., H. S., Z. Z., and Z. G. participated in optimizing the figures and assisted with material fabrication and characterization. All authors contributed to the analysis and discussion of the data.

## Conflicts of interest

There are no conflicts to declare.

## Data Availability

The data supporting this article have been included as part of the Supplementary Information.

View Article Online
DOI: 10.1039/D5MH01249J

**Acknowledgements**

The authors acknowledge the financial support from the National Natural Science Foundation of China (51973227, 22005011, 21633014, 51901009, 21988102, and 52322312), Beijing Natural Science Foundation (2232071), and the Fundamental Research Funds for the Central Universities.

**References**

1. Y. Q. Hou and X. Hou, *Science*, 2021, **373**, 628-629.
2. X. Zhang, B. Song and L. Jiang, *Acc. Chem. Res.*, 2022, **55**, 1195-1204.
3. Q. Ding, H. Wang, Y. Zhou, Z. Zhang, Y. Luo, Z. Wu, L. Yang, R. Xie, B.-R. Yang, K. Tao, S. Pan, F. Liu, J. Fu, F. Huo and J. Wu, *Adv. Mater.*, 2025, **37**, 2502369.
4. S. Zhang, J. Zhang, Y. Zhang and Y. Deng, *Chem. Rev.*, 2017, **117**, 6755-6833.
5. Y. Chen, Z. Zhu, Y. Tian and L. Jiang, *Exploration*, 2021, **1**, 20210101.
6. D. D. Lei, Z. Zhang and L. Jiang, *Chem. Soc. Rev.*, 2024, **53**, 2300-2325.
7. B.-Y. Liu, Y.-H. Zhang, Y. Qian, D. Quan, M.-J. Jia, X.-Y. Jin, M. Zhou, X.-Y. Kong and L. Jiang, *Angew. Chem., Int. Ed.*, 2024, **63**, e202317361.
8. Z. Deng, T. Wan, D. Chen, W. Ying, Y.-J. Zeng, Y. Yan and X. Peng, *Small*, 2020, **16**, 2002699.
9. Y. Xu, X. Sui, S. Guan, J. Zhai and L. Gao, *Adv. Mater.*, 2015, **27**, 1851-1855.
10. L. Wang, W. Zhang, J. Cao, S. Li, Y. Ma, Y. Meng, Y. Chen and L. Jiang, *Device*, 2024, **2**, 100293.
11. L. Wen, X. Zhang, Y. Tian and L. Jiang, *Sci. China Mater.*, 2018, **61**, 1027-1032.
12. F. Gonçalves, A. Ribeiro, C. Silva and A. Cavaco-Paulo, *Crit. Rev. Biotechnol.*, 2021, **41**, 441-455.
13. S. Firestein, *Nature*, 2001, **413**, 211-218.
14. Y. Kong, Y. Li, X. Cui, L. Su, D. Ma, T. Lai, L. Yao, X. Xiao and Y. Wang, *Nano Mater. Sci.*, 2022, **4**, 339-350.
15. M. Khatib and H. Haick, *ACS Nano*, 2022, **16**, 7080-7115.
16. S. M. Majhi, A. Mirzaei, H. W. Kim, S. S. Kim and T. W. Kim, *Nano Energy*, 2021, **79**, 105369.
17. R. Kumar, O. Al-Dossary, G. Kumar and A. Umar, *Nano-Micro Lett.*, 2015, **7**, 97-120.
18. Y. Ma, W. Li, W. Zhang, L. Kong, C. Yu, C. Tang, Z. Zhu, Y. Chen and L. Jiang, *Mater. Horiz.*, 2024, **11**, 3996-4014.

19. L. Wang, Y. Zhang, Y. Chen and L. Jiang, *ACS Nano*, 2024, **18**, 9043-9052.
20. Z. Fallah, E. N. Zare, M. A. Khan, S. Iftekhar, M. Ghomi, E. Sharifi, M. Tajbakhsh, N. Nikfarjam, P. Makvandi, E. Lichtfouse, M. Sillanpaa and R. S. Varma, *Adv. Colloid Interface Sci.*, 2021, **294**.
21. M. L. Jin, S. Park, H. Kweon, H. J. Koh, M. Gao, C. Tang, S. Y. Cho, Y. Kim, S. Y. Zhang, X. L. Li, K. Shin, A. P. Fu, H. T. Jung, C. W. Ahn and D. Kim, *Adv. Mater.*, 2021, **33**.
22. Z. Zhang, J. Li, H. Chen, H. Wang, Y. Luo, R. Si, R. Xie, K. Tao, B.-R. Yang, D. Zhang, F. Liu, F. Huo and J. Wu, *Adv. Funct. Mater.*, 2025, 2502583.
23. S. Kwon, Y. Pak, B. Kim, B. Park, J. Kim, G. Kim, Y.-R. Jo, S. Limbu, K. Stewart, H. Kim, B.-J. Kim, S.-Y. Jang, H. Kang, J.-W. Min, J.-S. Kim, G. Y. Jung and K. Lee, *J. Mater. Chem. A*, 2020, **8**, 16884-16891.
24. C. Esteves, S. I. C. J. Palma, H. M. A. Costa, C. Alves, G. M. C. Santos, E. Ramou, A. L. Carvalho, V. Alves and A. C. A. Roque, *Adv. Mater.*, 2022, **34**, 2107205.
25. W. Ying, K. Zhou, Q. Hou, D. Chen, Y. Guo, J. Zhang, Y. Yan, Z. Xu and X. Peng, *J. Mater. Chem. A*, 2019, **7**, 15062-15067.
26. H. Z. Dou, B. Jiang, M. Xu, Z. Zhang, G. B. Wen, F. F. Peng, A. P. Yu, Z. Y. Bai, Y. L. Sun, L. H. Zhang, Z. Y. Jiang and Z. W. Chen, *Angew. Chem., Int. Ed.*, 2019, **58**, 13969-13975.
27. W. Ying, J. S. Cai, K. Zhou, D. K. Chen, Y. L. Ying, Y. Guo, X. Q. Kong, Z. P. Xu and X. S. Peng, *ACS Nano*, 2018, **12**, 5385-5393.
28. C. Li, H. Liu, L. Xu, F. Zhao, J. Zhu, L. Wu, C. Yu, Y. Chen, Z. Zhu, C. Tang and L. Jiang, *Adv. Funct. Mater.*, 2025, **35**, 2418630.
29. C. Yu, L. Xu, F. Zhao, L. Kong, Y. Chen, L. Li, Z. Zhu and L. Jiang, *ACS Mater. Lett.*, 2024, **6**, 5454-5478.
30. Y. Zhang, J. Liu, C. Rong, D. Wang, W. Li, Z. Gao and Y. Chen, *Langmuir*, 2024, **40**, 18821-18836.
31. S. P. Lonkar, Y. S. Deshmukh and A. A. Abdala, *Nano Res.*, 2015, **8**, 1039-1074.
32. S. Leaper, A. Abdel-Karim, B. Faki, J. M. Luque-Alled, M. Alberto, A. Vijayaraghavan, S. M. Holmes, G. Szekely, M. I. Badawy, N. Shokri and P. Gorgojo, *J. Membr. Sci.*, 2018, **554**, 309-323.
33. H. Zhang, X. Wang and J. Wu, *Small*, 2012, **8**, 3775-3780.
34. T. Patil, S. Dharaskar, M. Sinha and S. S. Jampa, *Environ. Sci. Pollut. Res.*, 2022, **29**, 35723-35745.

View Article Online
DOI: 10.1039/D5MH01249J

35. X. Zhu, D. Liu, Q. Chen, L. Lin, S. Jiang, H. Zhou, J. Zhao and J. Wu, *Chem. Commun.*, 2016, **52**, 3042-3045.
36. H. Zhan, Z. Xiong, C. Cheng, Q. Liang, J. Z. Liu and D. Li, *Adv. Mater.*, 2020, **32**, 1904562.
37. K. R. Seddon, A. Stark and M.-J. Torres, *Pure Appl. Chem.*, 2000, **72**, 2275-2287.
38. J. Le Bideau, L. Viau and A. Vioux, *Chem. Soc. Rev.*, 2011, **40**, 907-925.
39. C. Comminges, R. Barhdadi, M. Laurent and M. Troupel, *J. Chem. Eng. Data*, 2006, **51**, 680-685.
40. X. Zhu, H. Zhang and J. Wu, *Sens. Actuators, B*, 2014, **202**, 105-113.
41. J. Halme, P. Vahermaa, K. Miettunen and P. Lund, *Adv. Mater.*, 2010, **22**, 210-234.
42. B. Zayat, P. Das, B. C. Thompson and S. R. Narayan, *J Phys. Chem. C*, 2021, **125**, 7533-7541.
43. H. Lim, H. Kwon, H. Kang, J. E. Jang and H.-J. Kwon, *Nano-Micro Lett.*, 2024, **16**.
44. F. Rahmani, P. Scovazzo, M. A. Pasquinelli and S. Nouranian, *ACS Appl. Mater. Interfaces*, 2021, **13**, 44460-44469.
45. M. Dong, K. Zhang, X. Wan, S. Wang, S. Fan, Z. Ye, Y. Wang, Y. Yan and X. Peng, *Small*, 2022, **18**, 2108026.
46. E. Pesis, *Postharvest. Biol. Technol.*, 2005, **37**, 1-19.
47. C. Rojas-Flores, R. I. Ventura-Aguilar, S. Bautista-Baños, S. Revah and J. O. Saucedo-Lucero, *Microbiol. Res.*, 2019, **228**, 126327.
48. L. A. Jurado, H. Kim, A. Rossi, A. Arcifa, J. K. Schuh, N. D. Spencer, C. Leal, R. H. Ewoldt and R. M. Espinosa-Marzal, *Phys. Chem. Chem. Phys.*, 2016, **18**, 22719-22730.
49. Y. Ye, H. Oguzlu, J. Zhu, P. Zhu, P. Yang, Y. Zhu, Z. Wan, O. J. Rojas and F. Jiang, *Adv. Funct. Mater.*, 2023, **33**, 2209787.
50. E. Feliziani, L. Landi and G. Romanazzi, *Carbohydr. Polym.*, 2015, **132**, 111-117.
51. J. F. Ayala-Zavala, S. Y. Wang, C. Y. Wang and G. A. González-Aguilar, *LWT--Food Sci. Technol.*, 2004, **37**, 687-695.
52. D. V. D. Spoel, E. Lindahl, B. Hess, G. Groenhof, A. E. Mark and H. J. Berendsen, *J. Comput. Chem.*, 2005, **26**, 1701-1718.
53. M. J. Abraham, T. Murtola, R. Schulz, S. Páll, J. C. Smith, B. Hess and E. Lindahl, *SoftwareX*, 2015, **1**, 19-25.
54. L. Martínez, R. Andrade, E. G. Birgin and J. M. Martínez, *J. Comput. Chem.*, 2009, **30**, 2157-2164.

55. W. L. Jorgensen, D. S. Maxwell and J. Tirado-Rives, *J. Am. Chem. Soc.*, 1996, **118**, 11225-11236.

56. T. Lu and F. Chen, *J. Comput. Chem.*, 2012, **33**, 580-592.

The data supporting this article have been included as part of the Supplementary Information.